Article

Surface Displacement of Hurd Rock Glacier from 1956 to 2019 from Historical Aerial Frames and Satellite Imagery (Livingston Island, Antarctic Peninsula)

Gonçalo Prates [1,2,3,*] and Gonçalo Vieira [1]

1   Centro de Estudos Geográficos, Associate Laboratory TERRA, Instituto de Geografia e Ordenamento do Território, Universidade de Lisboa, 1600-276 Lisboa, Portugal
2   Instituto Superior de Engenharia, Universidade do Algarve, 8005-139 Faro, Portugal
3   Laboratorio de Astronomía, Geodesia y Cartografía, Universidade de Cádiz, 11510 Cádiz, Spain
*   Correspondence: gprates@ualg.pt; Tel.: +351-289-800-100

Abstract: In the second half of the 20th century, the western Antarctic Peninsula recorded the highest mean annual air temperature rise in the Antarctic. The South Shetland Islands are located about 100 km northwest of the Antarctic Peninsula. The mean annual air temperature at sea level in this Maritime Antarctic region is close to -2 °C and, therefore, very sensitive to permafrost degradation following atmospheric warming. Among geomorphological indicators of permafrost are rock glaciers found below steep slopes as a consequence of permafrost creep, but with surficial movement also generated by solifluction and shallow landslides of rock debris and finer sediments. Rock glacier surface velocity is a new essential climate variable parameter by the Global Climate Observing System, and its historical analysis allows insight into past permafrost behavior. Recovery of 1950s aerial image stereo-pairs and structure-from-motion processing, together with the analysis of QuickBird 2007 and Pleiades 2019 high-resolution satellite imagery, allowed inferring displacements of the Hurd rock glacier using compression ridge-and-furrow morphology analysis over 60 years. Displacements measured on the rock glacier surface from 1956 until 2019 were from 7.5 m to 22.5 m and surface velocity of 12 cm/year to 36 cm/year, measured on orthographic images, with combined deviation root-mean-square of 2.5 m and 2.4 m in easting and northing. The inferred surface velocity also provides a baseline reference to assess today's displacements. The results show patterns of the Hurd rock glacier displacement velocity, which are analogous to those reported within the last decade, without being possible to assess any displacement acceleration.

Keywords: historical photogrammetry; structure-from-motion; rock glaciers; South Shetland Islands; Antarctic Peninsula

1. Introduction

Rock glaciers are debris landforms generated by the former or current creep of frozen ground (permafrost), detectable in the landscape due to front and lateral margins and generally ridge-and-furrow surface topography [1]. They result mainly from the deformation of permafrost under the influence of gravity via permafrost creep, with solifluction playing a role near the surface in the active layer, but also with the possibility of land-sliding. Rock glaciers have been widely used as a geomorphic indicator of permafrost and are landforms typical for the lower limit of permafrost in mountain regions, such as the European Alps [2]. Rock glacier surface velocities typically vary from centimeters up to a few meters per year. It depends on slope steepness, material properties, hydrology, and ground thermal conditions [3]. Rock glacier kinematics is forced by climate, with most rock glaciers accelerating following the warming of permafrost and resulting changes in rheology and hydrology in the debris masses [4]. Rock glacier velocity is hence a good proxy for the effects of climate change on permafrost, and its significance [5,6] is leading to its possible integration as an

associated parameter to the essential climate variable of permafrost in the Global Climate Observing System—World Meteorological Organization (WMO).

Contrary to mountainous regions worldwide, where rock glaciers have been a focus of research because they are significant for hazard assessment, hydrology (water supply), ecosystem niches, climate reconstruction, and climate change impacts [7–9], very little is known about rock glacier dynamics in the Antarctic. However, several rock glaciers have been identified in the South Shetland Islands (SSI), mainly on ice-free peninsulas of King George and Livingston islands, below 300 m above sea level (asl) [10]. Antarctic Peninsula rock glaciers with lengths of 55–470 m and widths of 100–360 m are small when compared to others in mountain environments worldwide. All those rock glaciers are active, three of them showing signs of recently reduced activity [10].

Rates of surface displacement of rock glaciers have barely been reported for the Antarctic Peninsula and the South Shetland Islands. One exception is the Hurd rock glacier in Livingston Island, where this study focuses. Studied by Interferometric Synthetic Aperture Radar (InSAR), its surface velocity was measured using phase-differential Global Navigation Satellite Systems (GNSS) with reported velocities of up to about 30 cm/year [11]. Rock glaciers can also be monitored using ground- or aerial-based photogrammetry, laser scanning, and visible-band satellite imagery [12]. Most data feeding these techniques may only be used for recent years. For the SSI, the historical aerial photogrammetric frames of the Falkland Islands and Dependencies Aerial Survey Expedition (FIDASE) from the 1950s [13,14] are possibly the oldest remote sensing data for the archipelago and are comparable to the decimeter-level pixel resolution of nowadays satellite imagery.

This study assesses the capability of extending monitoring back in time [15,16] to infer the Hurd rock glacier mean surface velocity with cm/year precision over 60 years, from 1956 to 2019. For this purpose, we used historical aerial frames and recent high-resolution satellite imagery.

2. Study Area

Since the 1950s, the western Antarctic Peninsula has suffered one of the highest maximum mean annual air temperature (MAAT) increases of the Antarctic, with as much as 3.4 °C, or about 0.5 °C/decade based on the Faraday/Vernadsky station record [17], placing the region as one of the world's climate warming hotspots [18–20]. Higher temperatures have been accompanied by increased precipitation [21,22] and higher snow accumulation, particularly in the western Antarctic Peninsula [23]. However, a regional cooling has been reported for the northwest Antarctica Peninsula from 1999 to 2015. Since then, the warming trend has resumed, with the summer of 2020 breaking record highs with maxima of 18.3 °C recorded at Esperanza Station [24]. In the SSI, about 100 km off the northwest Antarctic Peninsula (Figure 1a), the MAAT increased nearly 2 °C from 1968 until 2022 (Figure 1b). The MAAT is close to −2 °C at sea level [25], which makes the cryosphere very sensitive to small air temperature changes [26–28].

Permafrost is widespread in the Antarctic Peninsula, except close to sea level in its northwestern sector [29]. Modeling of the temperature at the top of permafrost shows that the SSI have permafrost temperatures above −2 °C, but frequently, just below freezing [28,30]. The comparison between the first measurements of the active layer thickness in the 1950s–60s and recent monitoring data has revealed an increase in the active layer depth in some areas of the SSI and Anvers Island [26,27]. Starting in 2000 and extending along the International Polar Year 2007–2008, a borehole network was installed, first in the SSI and later in the Antarctic Peninsula, measuring primarily permafrost temperature and active-layer thickness but also geomorphological changes [26–28,31–33]. Accompanying the reported atmospheric cooling, in some regions of the SSI, from 2006 to 2015, there has been a reduction of the active layer thickness at a rate of about 1.5–2.0 cm/year [31,32] and soil cooling as inferred from annual freezing indexes [34]. Lower summer temperatures have promoted a longer snow cover period [33,35], cooling the ground [25].
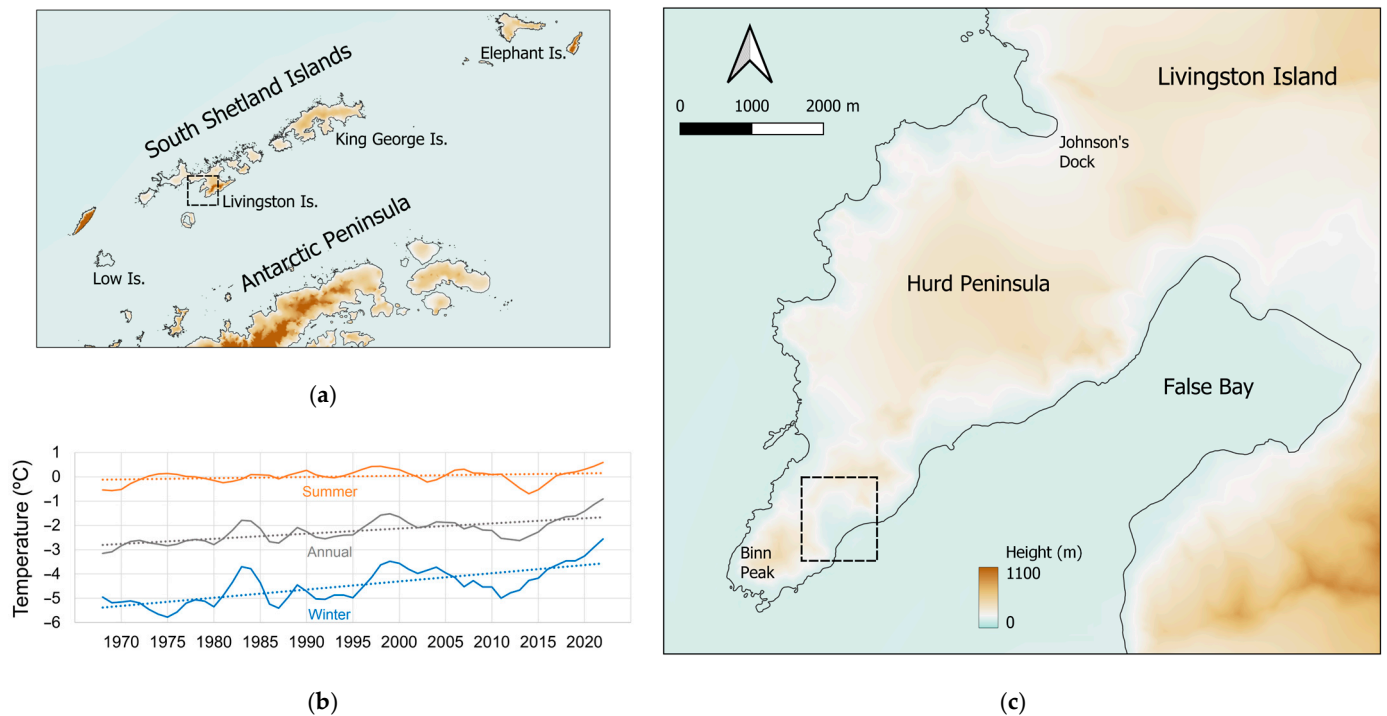
Figure 1. Location of Hurd Peninsula, within the dashed box, in Livingston Island of the South Shetland Islands about 100 km north of the Antarctic Peninsula (**a**). Air temperature at Bellingshausen station, King George Island, retrieved from Reference Antarctic Data for Environmental Research (legacy.bas.ac.uk/met/reader/) (accessed on 19 April 2023). Annual (gray), winter (blue), and summer (orange) means in solid line for weighted moving average and dotted line for trend (**b**). Location of Hurd rock glacier, inside the dashed box, in Hurd Peninsula with digital elevation model from historical aerial frames and REMA outside the SfM computed area (**c**).

No data has yet been published on the effects of the warming recorded since 2015 on permafrost temperatures and the active layer, but these are expected to warm and increase in thickness. In this paper, we study the Hurd rock glacier, which is located in a small glacial valley in the south of Hurd Peninsula in Livingston Island (Figure 1c). The bedrock is composed of sandstones, shales, and greywackes of the Myers Bluff Formation [10]. Binn Peak (392 m) is the highest summit on the ridge, with over 200 m elevation that bounds the valley. The rock glacier is formed by a debris accumulation about 470 m long and 360 m wide, with the surface showing longitudinal and transversal pressure ridges and furrows (Figure 2). The latter are especially present in the lower sector close to the front, which shows a maximum slope of 45° and is 15 to 20 m high [10]. The rock glacier forms in front of a small retreating cirque glacier and extends from about 110 m to 20 m asl, terminating over a fluvioglacial infill lying in contact with a raised marine terrace [36] about 150 m from the shoreline of False Bay. The glacial cirque headwalls the rock glacier with debris feeding the rock glacier, especially on the eastern side.

Permafrost in the Hurd Peninsula is continuous above about 150 m asl and absent in the raised beach terraces up to 30 m asl but is known to occur in relict bodies in ice-cored moraines, as well as in rock glaciers down to sea level [37]. Permafrost temperatures range from −0.4 to −1.8 °C, showing that it is very susceptible to thawing and generating thermokarst features in ice-rich terrain, but also debris flows and active-layer detachment slides [26–28]. The MAAT at sea level is about −1.2 °C and, in the short summer, rainfall events are frequent, and mean summer temperatures are 1.9 °C [38]. In Hurd rock glacier, the snow cover can melt completely in warm summers, but it is frequent that it prevails in furrows and sheltered areas.

Figure 2. Oblique photograph of Hurd rock glacier depicting the eastern valley slope and the ridge and furrows topography, as well as the frontal zone over the Holocene raised beach.

The first detailed research about Hurd rock glacier presented a geomorphological map and several vertical electrical soundings [36] that showed the presence of a high resistivity unit below a 1 to 3 m unfrozen superficial layer, having about 2 m thickness, and being interpreted as permafrost. The fluvioglacial plain in front of the rock glacier showed no permafrost, but the lobate debris features present in the slopes at the same elevation as the top of the rock glacier body suggested that its roots were in the continuous permafrost sector. The study of impacts of the atmosphere on phase delay for using InSAR to detect surface displacement of the rock glaciers in Livingston Island [11] refer to annual phase-differential GNSS data for the period of 2011 to 2015, which showed surface velocities at the Hurd rock glacier body of up to 30 cm/year, with faster sectors in the rock glacier front and central body and slower sectors in its eastern and western margins.

3. Materials and Methods

3.1. Structure from Motion and Rational Polynomial Processing

Classical stereo-photogrammetry is a mapping tool applied for almost one century, where from several overlapping images of the Earth's surface, both surface models and orthographic images are derived. The geometric consistency of the obtained information is appropriate for studying topographical changes and geomorphological dynamics [12].

Recently, structure from motion (SfM) was developed, being a near-automated compilation of digital imagery processing strategies that solves, together, camera position and surface geometry [39]. SfM's complete solution is based on the geometry of the photography and a highly redundant number of automatically detected matching features proportional to surface texture and image resolution identified in several images from diverse perspectives and preferably with a high degree of overlap [40]. Together with the ongoing increase in processing power, SfM made digital stereo-photogrammetry cost-effective, which gave a significant advance to the field [39,41,42].

Furthermore, by independently detecting and computing additional matching features on handy subsets of the overlapping images by multi-view stereo (MvS) processing, massive geometric data on dense point clouds allow for complete surface reconstruction [43]. The SfM-MvS together involves the detection of matching features in individual images, their coordinates being measured in the camera reference system, and the computation of camera and features' relative positions in a non-scaled arbitrary coordinate system. Therefore, ground control points or known camera centers' positions in an appropriate Earth reference

system are required to generate a dense point cloud and, from it, a surface mesh and surface reconstruction or digital elevation model.

The camera positions and digital elevation model are then needed to correct the displacement of each pixel in the images to form the orthographic image. The displacement of each pixel position is due to the projection of the feature by a non-vertical line-of-sight between the camera center and the feature, thus radial function of feature height [44]. Hence, the complete imagery processing can be performed with human intervention almost limited to the ground control points' identification [45].

In recent years, satellite imagery has also been acquired in stereo-pairs, but typically only a single image is acquired in each passage [44]. Similarly, orthographic images from satellite imagery require the sensor geometry, position, and digital elevation model to correct the displacement of each pixel due to feature height. The rational polynomial coefficients (RPC) models are commonly applied in satellite imagery to describe the acquisition process of its sensors without a camera geometry model. Handily, the coefficients of the RPC model of each satellite image are provided with them and enhanced using ground control points to relate surface coordinates to image coordinates by cubic polynomials [46,47]. To detect topographical changes and geomorphological dynamics, digital elevation models and orthographic images can be compared. The surface reconstruction is not obtainable from satellite single images; however, their orthographic images can be applied to quantify geomorphological dynamics [45].

3.2. Dataset Characteristics and Selection of Ground Control Points

Two sets of stereo-pairs of aerial frames of the Hurd Peninsula and two satellite single images were analyzed. The stereo-pairs made with a Fairchild metric camera were from 17 December 1956 and 26 December 1957, with a lens focal distance of 152.88 mm on the first and 153.19 mm on the second date. The flight altitudes were about 3960 m on the first and about 4115 m on the second date, with the subsequent scales of 1:26,000 and 1:27,000. The digital softcopies' pixel length is about 0.02 mm on the hardcopy frame (1016 dpi), standard panchromatic-film grain resolution [44], and about 0.6 m on the Earth's surface.

Two satellite single images from 7 February 2007 and 28 February 2019, respectively taken by QuickBird and Pleiades sensors, with pixel length resolution better than 0.6 m in panchromatic mode, were also used. Hence, the initial estimated resolutions of all digital images involved were similar (Table 1).

Table 1. Applied imagery material information.

Proprietary	Type and Details	Number of Frames/Images	Altitude and Scale	Date
Falkland Islands and Dependencies Aerial Survey Expedition (FIDASE)	f: 152.9 mm f: 153.2 mm	4	3960 m 1:26,000	17 December 1956
		4	4115 m 1:27,000	26 December 1957
DigitalGlobe (QuickBird)	panchromatic 4 bands f: 8800.0 mm	1	450,000 m	7 February 2007
CNES/Airbus (Pleiades)	panchromatic 4 bands f: 12,905.0 mm	1	694,000 m	28 February 2019

Additional topographic data was accessed on the Reference Elevation Model of Antarctica (REMA) 2 m resolution digital elevation model. REMA was constructed from several individual stereoscopic digital elevation models extracted from pairs of submeter resolution satellite imagery acquired between 2009 and 2021 and vertically registered to satellite altimetry measurements, resulting in absolute uncertainties of less than 1 m and relative uncertainties of decimeters [48].

Apart from the selection of a few parameters, the identification of the ground control points was the main human intervention in the image processing and the main potential error source. Because of mobility and security reasons, it was not possible to survey these points with phase-differential GNSS, except on the rock glacier surface. Further, the lack of artificial ground control points was a strong limitation, as the interpretation of natural ground control points can be somewhat ambiguous, making it less crucial to survey with phase-differential GNSS precision. Nonetheless, phase-differential GNSS accuracy is expected to impact the overall precision of the orthographic images [45].

Scale and reference frame are the main purposes of ground control points, and hence, the same was used in all orthographic images to minimize the effect of a possible reference frame bias when differentiating them to quantify displacements and also accounting for the maximum height difference to constrain vertical scale. Their precision influence on the horizontal scale and reference frame rotation is inversely proportional to the distance between them, as for larger distances, lesser inaccuracy in reference frame rotation and scale is imposed. The required lens and frame centering, optional lens distortion, frame aspect, and skew calibration are adjusted to the scaled surface model and hence also affected by the ground control points precision.

While satellite images were processed by the ENVI 5.2 software with their rational polynomial coefficients and REMA digital elevation model, stereo-pairs were processed by the PhotoScan 1.0 software with SfM-MvS strategies.

The 2007 QuickBird satellite image was orthorectified with their RCP and the REMA model only and pan-sharpened (Figure 3a). This orthographic image was chosen as the reference for co-registration, from where coordinates in the World Geodetic System 84 reference system and projected in Universal Transverse Mercator at fuse 20 South were retrieved. Height was retrieved from the REMA model. Nine well-identified features in the historical aerial frames and satellite images, mostly at rock outcrops and dispersed locations (Figure 3a), were selected as ground control points in the common area to the aerial frames and satellite images. The 2019 Pleiades satellite image was then orthorectified with their RCP, the REMA model, and nine ground control points to be co-registered to the QuickBird orthographic image and pan-sharpened (Figure 3b).

Historical aerial frames were processed together: three stereo-pairs from 17 December 1956 and three stereo-pairs from 26 December 1957, totaling eight frames, and the nine ground control points, to generate a common dense point cloud and digital elevation model with 2.6 m resolution (Figure 1c). All stereo-pairs were processed together to increase the degree of overlap and, therefore, increase the common digital elevation model precision, also increasing the constraint in the co-registration of both orthographic images. The 1956 and 1957 orthographic images were generated from each date single frame with its center closer to the rock glacier (Figure 4a,b), which is the area where features are less affected by radial displacement due to ground height.

(**a**)
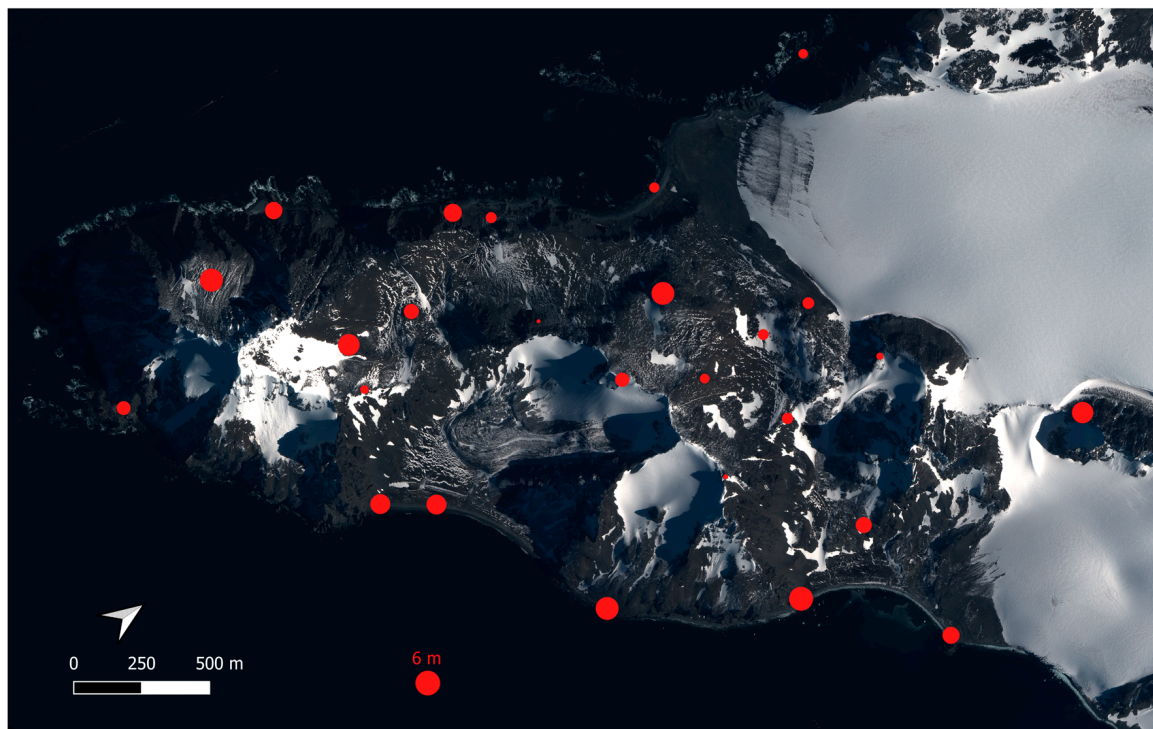
(**b**)

Figure 3. Orthographic image of 2007 by QuickBird sensor (©DigitalGlobe Inc., Boulder, Colorado, USA, 2007) with the location of the ground control points used shown in red circles (see Appendix A) and profile (A-B-C) of measured heights comparison (**a**). Orthographic image of 2019 by Pleiades sensor (©CNES, Paris, France, 2019, Airbus distribution service) with the location of the twenty-six assessed features and their orthographic images (1956, 1957, 2007, and 2019) coordinates' common deviation root-mean-squared (rms), varying from 0.9 m to 6.2 m (see Appendix B) (**b**).
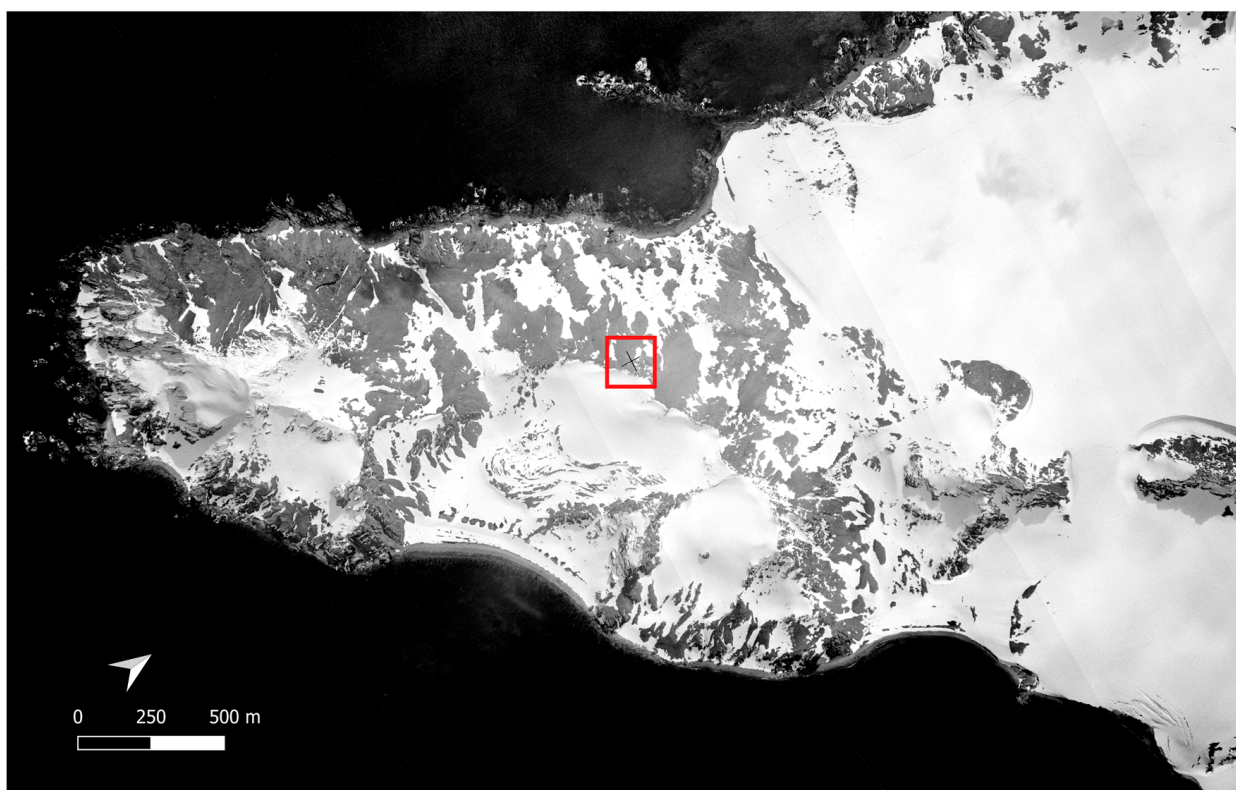
(**a**)
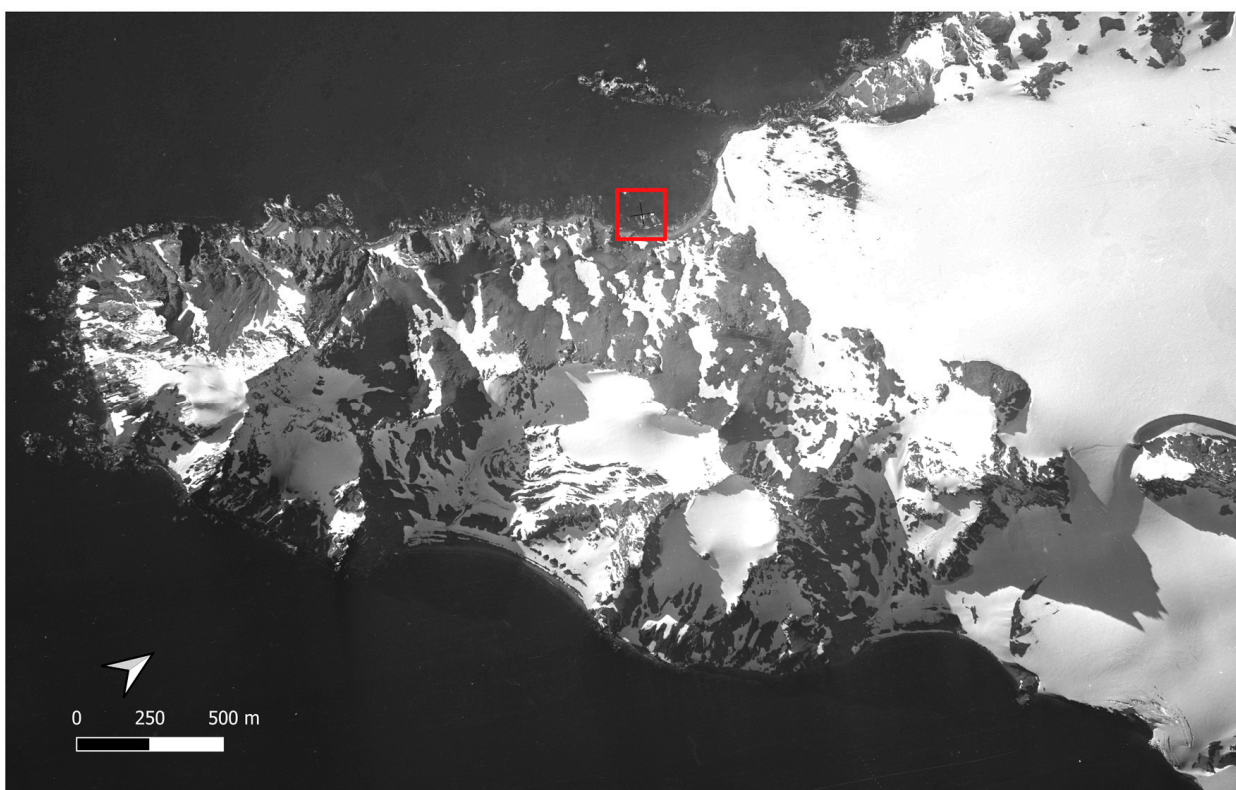
(**b**)

Figure 4. Orthographic image of 1956 and location of the frame center in a red box (**a**). Orthographic image of 1957 and location of the frame center in a red box (**b**).

4. Results

Orthographic Images Generation and Combined Accuracy Assessment

The orthographic 2019 Pleiades satellite image was co-registered to the 2007 QuickBird orthographic image with a deviation root-mean-squared (rms) of 3.4 m and 2.4 m in easting and northing, respectively, at the nine ground control points. The 1956 and 1957 historical aerial frames processed together gave a deviation rms of 2.1 m, 3.1 m, and 5.6 m in easting, northing, and height, respectively, at the nine ground control points.

Furthermore, to assess the relative accuracy among all orthographic images, twenty-six features were selected based on their expected immobility (Figure 3b). The coordinates of each feature were measured in every orthographic image, and their deviation rms were computed. The identification of corresponding features can be ambiguous and was minimized by avoiding steep terrain, shadows, and snow. Still, to evenly disperse the analyzed features throughout the orthographic images, this criterium was not always achieved, particularly due to shadows in the 1957 and 2019 orthographic images covering most of the southeast coastline (Figures 3b and 4b). A common deviation rms of all orthographic images (1956, 1957, 2007, and 2019) of 2.5 m and 2.4 m in easting and northing, respectively, was computed. The deviation rms computed at each feature is shown in Figure 3b, where 0.3 m and 6.0 m (easting) and 0.6 m and 4.6 m (northing) were the extreme values.

5. Discussion

Hurd Rock Glacier Surface Velocity

The controls of climate on rock glacier displacement have been analyzed by several authors, and rock glacier acceleration has been shown to be a consequence of climate warming in many cases [4]. However, other environmental factors control rock glacier displacements, such as variable sediment and ice/water supply to the rock glacier body. All these require being interpreted carefully and framed within the geomorphological and climate setting of each rock glacier. In steep and thin rock glaciers, rapid impact from atmospheric warming on rock glacier temperatures and creep are expected, while thicker rock glaciers may need decades for deformation to occur [3].

From the orthographic images of 1956, 1957, 2007, and 2019, mean displacement velocities can be measured at the rock glacier and the moraine at its root over nearly 60 years. As the rock glacier develops from nearly 100 m asl, north, to nearly 10 m asl, south, its gravity-driven displacement is expected mainly from north to south, and the features that best serve to measure it are the pressure ridges not covered by snow and with a nearly east–west direction (Figures 5 and 6). Due to different conditions of snow cover and illumination, no automatic inference of displacements was possible. These different conditions were useful to visually select common features on the rock glacier, for which displacement was inferred, as the identification of individual ridges benefits from furrows covered by snow and by the lack of shadows over the rock glacier. In Figures 5 and 6, the displacement vectors can be depicted, where their initial points are at the measured features in 1956 and 1957 (Figure 5) while their terminal points are at these features in 2007 and 2019 (Figure 6), allowing for their identification in each orthographic image.

The southward displacement is measured with uncertainty mainly from the northing component. Over 60 years, the deviation rms of 2.4 m in northing implies a north-to-south displacement velocity uncertainty of 4 cm/year. For achieving a 95% confidence level, only north-to-south displacements above 4.7 m were considered. All displacements were measured via the difference of corresponding features' coordinates in each pair of orthographic images of 1956 with 2007 and 2019, and 1957 with 2007 and 2019. Therefore, the average displacement velocities have an uncertainty of about 2 cm/year.

Displacements measured on the rock glacier surface vary between 7.5 m and 22.5 m, and the corresponding surface velocity values were from 12 cm/year to 36 cm/year for the period of 1956 to 2019, with the fastest sectors being the eastern front sector, as well as the front moraine at the root of the rock glacier.
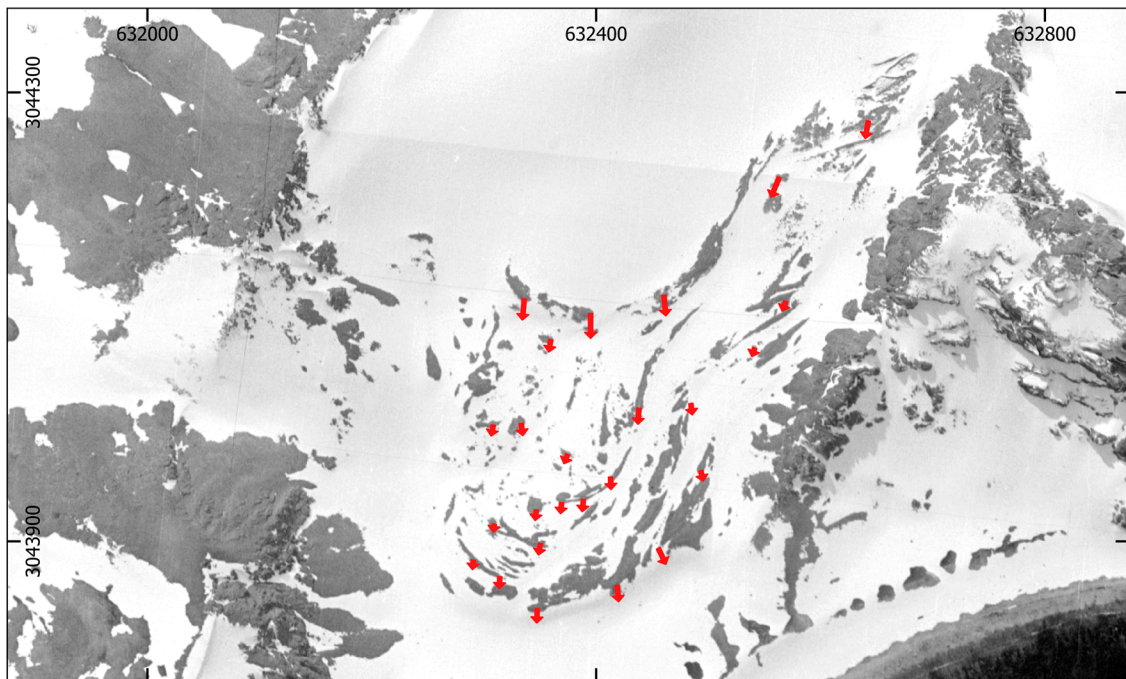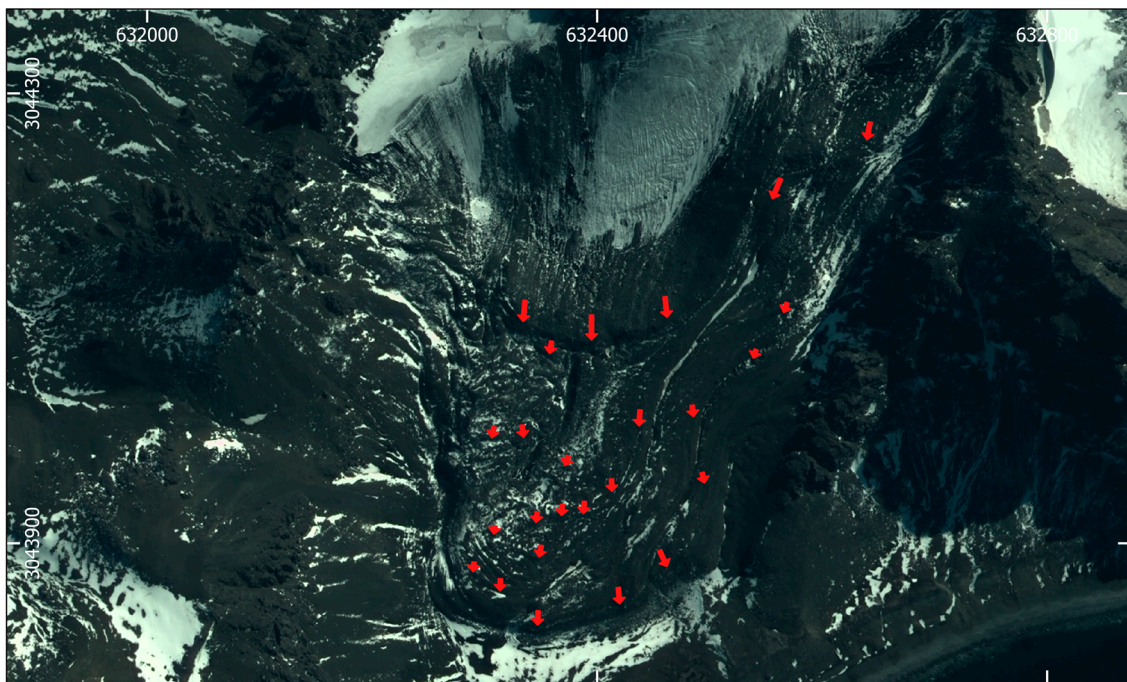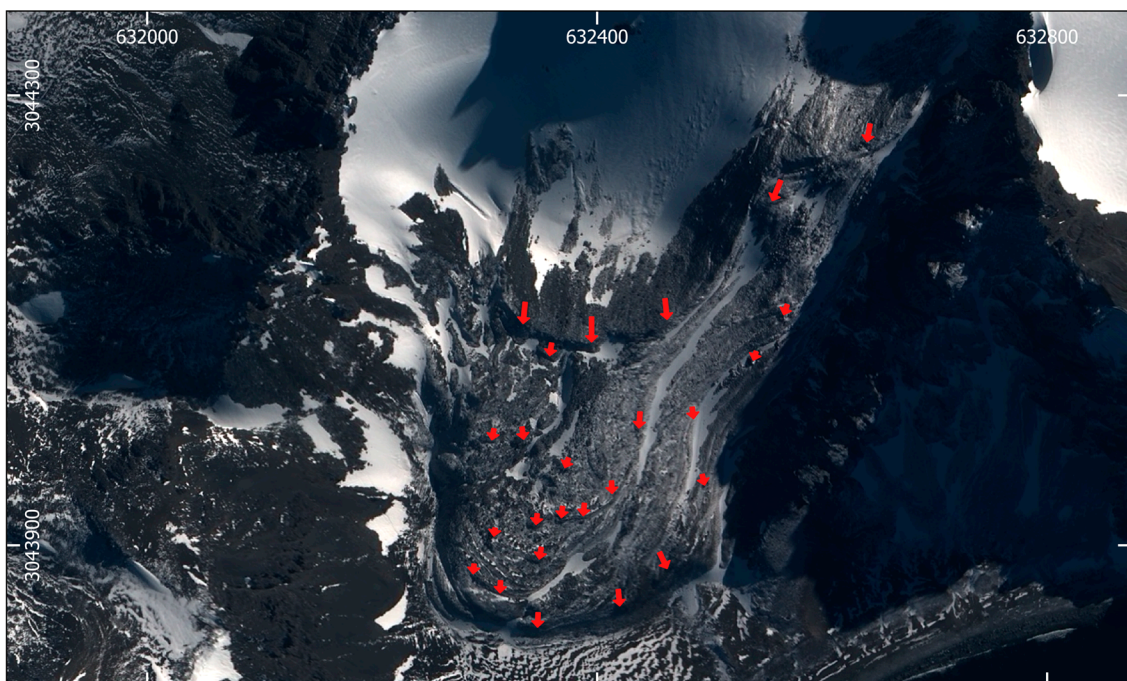
(**a**)
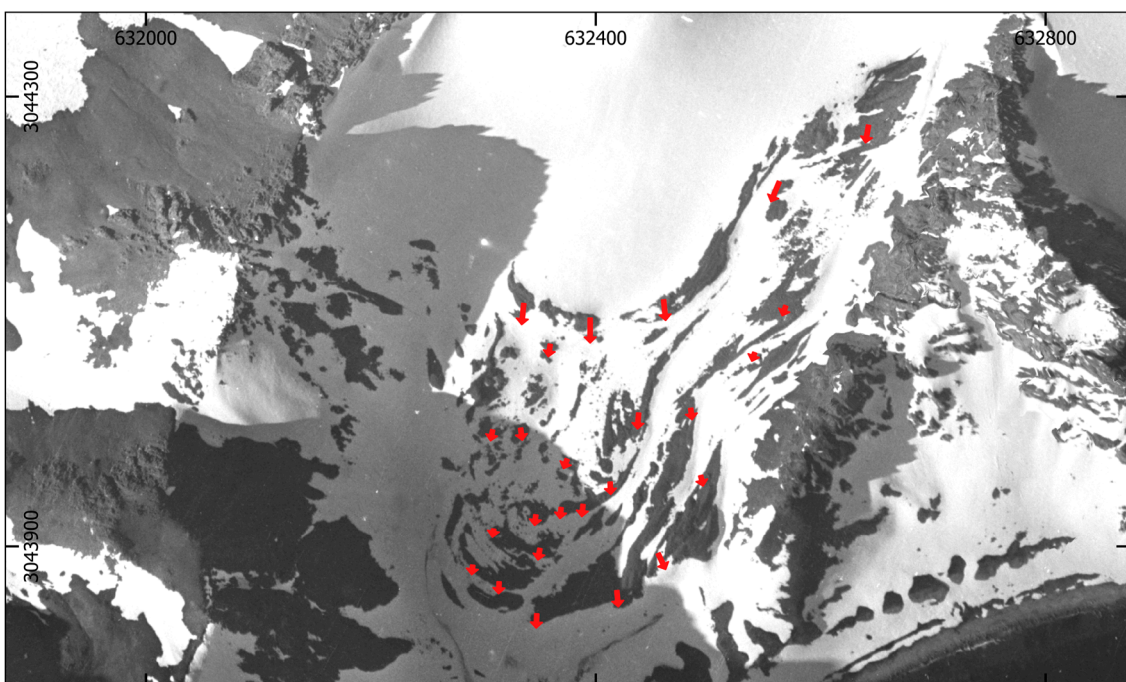
(**b**)

Figure 5. Initial point of displacement and displacement vectors (in red) at the measured features in 1956 (**a**) and 1957 (**b**). Displacement vectors in image scale range from 7.5 m to 22.5 m. Coordinates in WGS84–UTM20S.

(**a**)

(**b**)

Figure 6. Terminal point of displacement and displacement vectors (in red) at the measured features in 2007 (©DigitalGlobe Inc., Boulder, Colorado, USA, 2007) (**a**) and 2019 (©CNES, Paris, France, 2019, Airbus distribution service) (**b**). Displacement vectors in image scale range from 7.5 m to 22.5 m. Coordinates in WGS84–UTM20S.

The highest displacement velocities were measured at the front moraine at the root of the rock glacier, ranging from 29 cm/year to 36 cm/year (Figure 7). The lower displacement velocity values were measured at the western sector of the rock glacier body, ranging from 12 cm/year to 18 cm/year. At the eastern sector of the rock glacier body and its front, the displacement velocity ranges from 21 cm/year to 26 cm/year. Any displacement could be

detected on the rock glacier for the very short interval of 1956 to 1957. No displacement was detected greater than 4.7 m from 2007 to 2019 (Figure 6). This measured velocity field agrees well with that measured by phase-differential GNSS and reported within the last decade [6], not allowing for a clear assessment of any displacement acceleration.
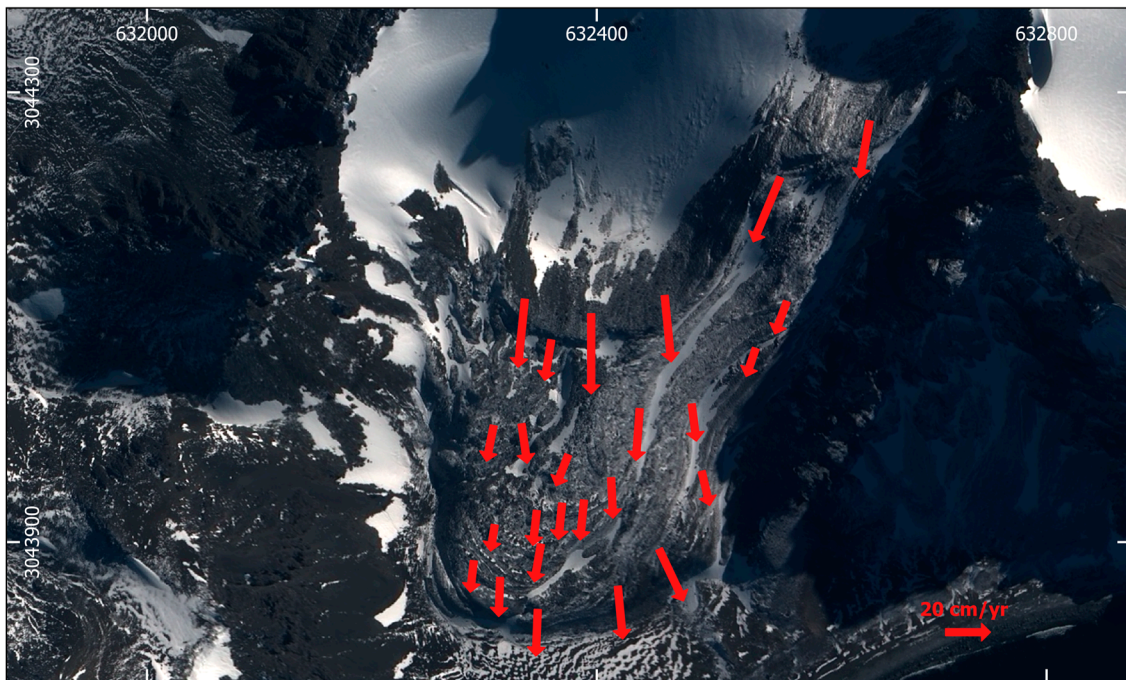

Figure 7. Surface velocities of displaced features range from 12 cm/year to 36 cm/year. Initial point of velocity vectors (in red) at the measured features in 1956. Includes material ©CNES, Paris, France, 2019 (Airbus distribution service). Coordinates in WGS84–UTM20S.

Although the height precision obtained from SfM applied to the 1956 and 1957 photographic images was inferred at about 5.6 m, the height profile relative to the 2021 REMA digital model (Figure 8) reveal high agreement between them, both above the rock glacier (A–B), over the rock glacier and its adjacent raised beach (B–C). Horizontal displacements at the rock glacier root can be measured at about 10–20 m between profile inflections, although displacement at the rock glacier foot is less clear, perhaps smoothed by the snow accumulation at the 1956 and 1957 images. At the eastern sector of the rock glacier, a slight surface uplift may have taken place, extending to a small, elevated terrace at the raised beach. Yet, these differences may be associated to the limited vertical precision.

The Hurd rock glacier rheology and evolution of its permafrost thermal state are unknown, limiting its surface velocity modeling. The regional temperature evolution at the South Shetland Islands may be assessed by analyzing the MAAT time series of Bellingshausen station in King George Island (Figure 1b). MAAT shows an increase of about 1.5 °C from 1967 to 1999, followed by a decrease of about −1.0 °C until 2014, and again by an increase of about 1.5 °C in MAAT until 2022 (Figure 1b). Despite the significant atmospheric warming reported for the archipelago, since at least the 1950s, the measured displacement velocities do not show a clear acceleration, as could be expected following the warming in the climate series. This may be due to the very warm setting of the Hurd rock glacier in the permafrost zone of the South Shetland, below the continuous permafrost [23]. Furthermore, the complex interannual variability in snow cover conditions [30], with poorly understood impacts on ground hydrology, may add extra complexity to the understanding of Hurd rock glacier rheology as well as its reaction to climate change.
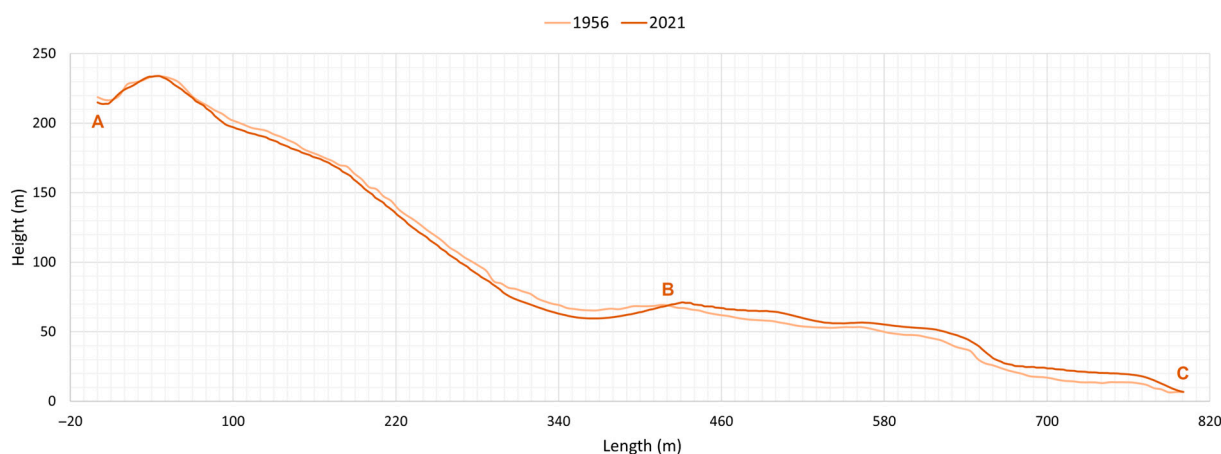
Figure 8. Height profile of the Hurd Rock Glacier in 1956 based on SfM from 1956 and 1957 FIDASE photographic data relative to the 2021 REMA from satellite imagery from 2009 to 2021. A-B-C location in the profile as in Figure 3a.

6. Conclusions

The analysis of co-registered high-resolution satellite orthographic images from 2007 and 2019 together and orthographic images generated from SfM-MvS processed stereo-pairs from 1956 and 1957 shows that historical photogrammetric frames allow developing detailed surface deformation monitoring studies in remote Antarctic areas. This is the first time that long-term displacement velocities for rock glaciers are presented for the Antarctic Peninsula and the South Shetland Islands region, which makes this data especially valuable and shows the potential applicability of the technique and datasets used.

Results depict that the analysis of historical aerial frames of the South Shetland Islands from the 1950s provides reliable information for the analysis of geomorphological changes with considerable resolution. Nevertheless, this type of analysis requires a sufficient time span to accommodate its uncertainty level. In this study, the 1950s stereo-pairs recovery and SfM-MvS processing allowed inferring displacements of the Hurd rock glacier compression ridges over 60 years. Orthographic images' precision can be enhanced by ground control points with accurate coordinates at least one order of magnitude above the images' resolution, measured by phase-differential GNSS. The uncertainty of the produced orthographic images was 2.5 m and 2.4 m in easting and northing, respectively.

At the Hurd rock glacier, displacement velocities were measured over about 60 years, ranging from 12 cm/year to 36 cm/year, depending on the rock glacier sector. These values reveal a similar spatial distribution to that reported from short phase-differential GNSS time series within the last decade. From 2007 to 2019, no displacement surpassing the displacement uncertainty on the orthographic images was detected. Jointly, these statements support the long-term strength and the short-term limitation of visible-band imagery to detect ground displacements. The implemented strategy, where no automatic co-registration with local adjustment of features and additional pixel displacements to those acknowledged for camera and central projection geometry, showed to be trustworthy at metric-level, avoiding spurious diminished to null displacements. The orthographic image data did not allow for detecting changes in the Hurd rock glacier displacement velocities above the inferred 4 cm/year uncertainty when compared to reported short time series of phase-differential GNSS measurements at this time, following the recorded atmospheric warming of the South Shetland region.

Author Contributions: Conceptualization, G.P. and G.V.; formal analysis, G.P.; funding acquisition, G.V.; methodology, G.P.; resources, G.P. and G.V.; validation, G.P.; visualization, G.P.; writing—original draft, G.P.; writing—review and editing, G.P. and G.V. All authors have read and agreed to the published version of the manuscript.

Data Availability Statement: Not applicable.

Conflicts of Interest: The authors declare no conflict of interest. The founding sponsors had no role in the design of the study, in the collection, analysis, or interpretation of data, in the writing of the manuscript, or in the decision to publish the results.
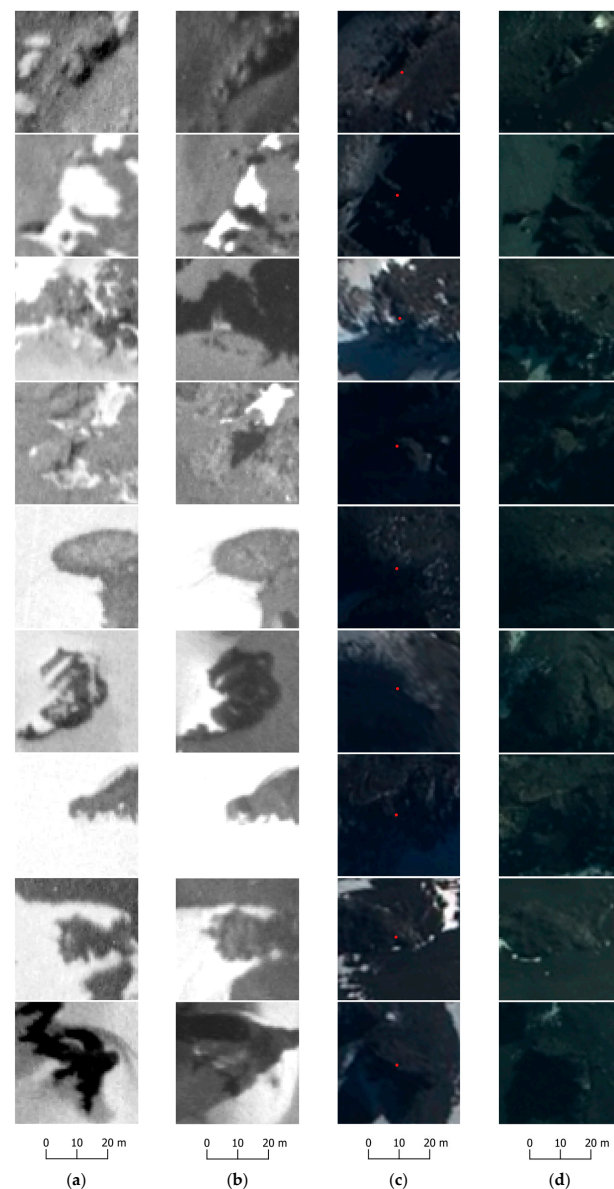
Appendix A

Figure A1. Georeferencing ground control points' (red dots) at orthographic images of 1956 (**a**), 1957 (**b**), 2007 (©DigitalGlobe Inc., Boulder, Colorado, USA, 2007) (**c**) and 2019 (©CNES, Paris, France, 2019, Airbus distribution service) (**d**) for assessment of visual identification and relative precision.

Appendix B

Table A1. Coordinates of ground control points for precision assessment in WGS84-UTM20S.

1956		1957		2007		2019	
X (m)	Y (m)	X (m)	Y (m)	X (m)	Y (m)	X (m)	Y (m)
631,523.445	3,042,909.857	631,525.561	3,042,907.211	631,526.818	3,042,912.039	631,528.406	3,042,913.098
631,253.305	3,043,775.044	631,253.570	3,043,774.780	631,253.702	3,043,777.227	631,249.733	3,043,782.783
631,980.248	3,043,675.958	631,981.306	3,043,674.899	631,981.835	3,043,675.098	631,981.571	3,043,679.066
632,141.908	3,044,346.610	632,142.437	3,044,346.081	632,142.173	3,044,346.081	632,142.702	3,044,347.801
633,005.111	3,044,584.801	633,006.170	3,044,585.066	633,005.773	3,044,586.323	633,006.831	3,044,584.206
631,986.598	3,044,978.171	631,989.508	3,044,979.626	631,986.333	3,044,977.377	631,984.216	3,044,979.494
632,971.906	3,045,301.359	632,971.377	3,045,303.740	632,971.245	3,045,304.137	632,969.393	3,045,303.873
633,962.506	3,044,934.382	633,962.241	3,044,935.176	633,965.549	3,044,927.900	633,961.051	3,044,929.223
632,358.205	3,043,488.633	632,358.999	3,043,486.384	632,364.158	3,043,479.174	632,359.925	3,043,484.730
631,730.481	3,044,419.834	631,731.539	3,044,419.305	631,733.656	3,044,420.032	631,730.481	3,044,424.001
632,490.894	3,044,479.630	632,490.629	3,044,478.571	632,489.174	3,044,480.754	632,496.053	3,044,476.851
632,475.812	3,043,658.892	632,478.194	3,043,658.495	632,480.839	3,043,650.161	632,480.046	3,043,653.071
631,336.120	3,043,439.685	631,336.649	3,043,439.949	631,331.952	3,043,442.331	631,327.984	3,043,447.887
631,848.618	3,043,978.906	631,846.765	3,043,978.376	631,848.948	3,043,978.906	631,844.979	3,043,984.991
631,639.861	3,044,313.074	631,640.390	3,044,311.222	631,641.515	3,044,312.016	631,634.900	3,044,318.366
631,807.607	3,043,727.287	631,806.813	3,043,725.435	631,815.875	3,043,720.672	631,813.229	3,043,725.699
632,669.487	3,044,727.213	632,671.869	3,044,726.949	632,669.950	3,044,725.824	632,666.775	3,044,728.206
633,441.938	3,044,906.270	633,441.872	3,044,902.037	633,446.106	3,044,899.920	633,444.518	3,044,898.862
631,900.079	3,045,711.331	631,899.021	3,045,710.273	631,896.441	3,045,711.662	631,895.383	3,045,710.868
633,577.802	3,045,792.426	633,573.833	3,045,795.138	633,569.600	3,045,798.048	633,567.483	3,045,796.395
632,323.677	3,044,774.706	632,322.619	3,044,776.294	632,316.798	3,044,770.870	632,321.560	3,044,781.982
632,663.402	3,045,197.378	632,662.608	3,045,197.180	632,662.608	3,045,197.709	632,658.110	3,045,200.288
632,657.449	3,045,001.454	632,661.021	3,044,998.742	632,660.095	3,044,997.022	632,657.713	3,044,997.882
632,959.074	3,044,894.364	632,960.926	3,044,895.422	632,964.762	3,044,892.313	632,961.984	3,044,894.033
633,146.680	3,043,955.199	633,150.120	3,043,956.787	633,152.501	3,043,947.791	633,153.824	3,043,948.585
633,530.591	3,044,556.862	633,528.739	3,044,554.216	633,539.322	3,044,548.660	633,534.057	3,044,554.102

References

1.　RGIK. *Towards Standard Guidelines for Inventorying Rock Glaciers: Baseline Concepts (Version 4.2.2)*; IPA Action Group Rock Glacier Inventories and Kinematics: Troms and Finnmark, Norway, 2022; 13p.

2.　Haeberli, W. *Creep of Mountain Permafrost: Internal Structure and Flow of Alpine Rock Glaciers*; Eidgenössische Technische Hochschule Zürich: Zürich, Switzerland, 1985; Volume 77, 142p.

3.　Müller, J.; Vieli, A.; Gärtner-Roer, I. Rock Glaciers on the Run—Understanding Rock Glacier Landform Evolution and Recent Changes from Numerical Flow Modeling. *Cryosphere* **2016**, *10*, 2865–2886. [CrossRef]

4.　Marcer, M.; Cicoira, A.; Cusicanqui, D.; Bodin, X.; Echelard, T.; Obregon, R.; Schoeneich, P. Rock Glaciers throughout the French Alps Accelerated and Destabilised since 1990 as Air Temperatures Increased. *Commun. Earth Environ.* **2021**, *2*, 81. [CrossRef]

5.　Sorg, A.; Kääb, A.; Roesch, A.; Bigler, C.; Stoffel, M. Contrasting Responses of Central Asian Rock Glaciers to Global Warming. *Sci. Rep.* **2015**, *5*, 8228. [CrossRef]

6.　Rangecroft, S.; Suggitt, A.J.; Anderson, K.; Harrison, S. Future Climate Warming and Changes to Mountain Permafrost in the Bolivian Andes. *Clim. Change* **2016**, *137*, 231–243. [CrossRef] [PubMed]

7.　Reinosch, E.; Gerke, M.; Riedel, B.; Schwalb, A.; Ye, Q.; Buckel, J. Rock Glacier Inventory of the Western Nyainqêntanglha Range, Tibetan Plateau, Supported by InSAR Time Series and Automated Classification. *Permafr. Periglac. Process.* **2021**, *32*, 657–672. [CrossRef]

8.　Tielidze, L.G.; Cicoira, A.; Nosenko, G.A.; Eaves, S.R. The First Rock Glacier Inventory for the Greater Caucasus. *Geosciences* **2023**, *13*, 117. [CrossRef]

9.　Wagner, T.; Pleschberger, R.; Kainz, S.; Ribis, M.; Kellerer-Pirklbauer, A.; Krainer, K.; Philippitsch, R.; Winkler, G. The First Consistent Inventory of Rock Glaciers and Their Hydrological Catchments of the Austrian Alps. *Austrian J. Earth Sci.* **2020**, *113*, 1–23. [CrossRef]

10.　Serrano, E.; López-Martínez, J. Rock Glaciers in the South Shetland Islands, Western Antarctica. *Geomorphology* **2000**, *35*, 145–162. [CrossRef]

11.　Reis, A.R.; Catalao, J.; Vieira, G.; Nico, G. Mitigation of Atmospheric Phase Delay in InSAR Time Series Using ERA-Interim Model, GPS and MODIS Data: Application to the Permafrost Deformation in Hurd Peninsula, Antarctica. In Proceedings of the 2015 IEEE International Geoscience and Remote Sensing Symposium (IGARSS), Milan, Italy, 26–31 July 2015; pp. 3454–3457.

12. Kääb, A.; Vollmer, M. Surface Geometry, Thickness Changes and Flow Fields on Creeping Mountain Permafrost: Automatic Extraction by Digital Image Analysis. *Permafr. Periglac. Process.* **2000**, *11*, 315–326. [CrossRef]
13. Gavin-Robinson, C. The story of the Falkland Island dependencies aerial survey expeditions. *Flight* **1957**, 802–805.
14. Fox, A.J.; Cziferszky, A. Unlocking the Time Capsule of Historic Aerial Photography to Measure Changes in Antarctic Peninsula Glaciers. *Photogramm. Rec.* **2008**, *23*, 51–68. [CrossRef]
15. Tanguy, R.; Whalen, D.; Prates, G.; Vieira, G. Shoreline Change Rates and Land to Sea Sediment and Soil Organic Carbon Transfer in Eastern Parry Peninsula from 1965 to 2020 (Amundsen Gulf, Canada). *Arct. Sci.* **2023**. [CrossRef]
16. Tanguy, R.; Whalen, D.; Prates, G.; Pina, P.; Freitas, P.; Bergstedt, H.; Vieira, G. Permafrost Degradation in the Ice-Wedge Tundra Terrace of Paulatuk Peninsula (Darnley Bay, Canada). *Geomorphology* **2023**, *435*, 108754. [CrossRef]
17. Turner, J.; Barrand, N.E.; Bracegirdle, T.J.; Convey, P.; Hodgson, D.A.; Jarvis, M.; Jenkins, A.; Marshall, G.; Meredith, M.P.; Roscoe, H.; et al. Antarctic Climate Change and the Environment: An Update. *Polar Rec.* **2014**, *50*, 237–259. [CrossRef]
18. Vaughan, D.G.; Marshall, G.J.; Connolley, W.M.; Parkinson, C.; Mulvaney, R.; Hodgson, D.A.; King, J.C.; Pudsey, C.J.; Turner, J. Recent rapid regional climate warming on the Antarctic Peninsula. *Clim. Change* **2003**, *60*, 243–274. [CrossRef]
19. Turner, J.; Colwell, S.R.; Marshall, G.J.; Lachlan-Cope, T.A.; Carleton, A.M.; Jones, P.D.; Lagun, V.; Reid, P.A.; Iagovkina, S. Antarctic Climate Change during the Last 50 Years. *Int. J. Climatol.* **2005**, *25*, 279–294. [CrossRef]
20. Turner, J.; Bindschadler, R.; Convey, P.; di Prisco, G.; Fahrbach, E.; Gutt, J.; Hodgson, D.; Mayewski, P.; Summerhayes, C. *Antarctic Climate Change and the Environment*; Scientific Committee on Antarctic Research: Cambridge, UK, 2009.
21. Turner, J.; Lachlan-Cope, T.; Colwell, S.; Marshall, G.J. A Positive Trend in Western Antarctic Peninsula Precipitation over the Last 50 Years Reflecting Regional and Antarctic-Wide Atmospheric Circulation Changes. *Ann. Glaciol.* **2005**, *41*, 85–91. [CrossRef]
22. Miles, G.M.; Marshall, G.J.; McConnell, J.R.; Aristarain, A.J. Recent Accumulation Variability and Change on the Antarctic Peninsula from the ERA40 Reanalysis. *Int. J. Climatol.* **2008**, *28*, 1409–1422. [CrossRef]
23. Thomas, E.R.; Marshall, G.J.; McConnell, J.R. A Doubling in Snow Accumulation in the Western Antarctic Peninsula since 1850. *Geophys. Res. Lett.* **2008**, *35*, L01706. [CrossRef]
24. González-Herrero, S.; Barriopedro, D.; Trigo, R.M.; López-Bustins, J.A.; Oliva, M. Climate Warming Amplified the 2020 Record-Breaking Heatwave in the Antarctic Peninsula. *Commun. Earth Environ.* **2022**, *3*, 122. [CrossRef]
25. Oliva, M.; Navarro, F.; Hrbáček, F.; Hernández, A.; Nývlt, D.; Pereira, P.; Ruiz-Fernández, J.; Trigo, R. Recent Regional Climate Cooling on the Antarctic Peninsula and Associated Impacts on the Cryosphere. *Sci. Total Environ.* **2017**, *580*, 210–223. [CrossRef] [PubMed]
26. Vieira, G.; Bockheim, J.; Guglielmin, M.; Balks, M.; Abramov, A.A.; Boelhouwers, J.; Cannone, N.; Ganzert, L.; Gilichinsky, D.A.; Goryachkin, S.; et al. Thermal State of Permafrost and Active-Layer Monitoring in the Antarctic: Advances during the International Polar Year 2007-2009. *Permafr. Periglac. Process.* **2010**, *21*, 182–197. [CrossRef]
27. Bockheim, J.; Vieira, G.; Ramos, M.; López-Martínez, J.; Serrano, E.; Guglielmin, M.; Wilhelm, K.; Nieuwendam, A. Climate Warming and Permafrost Dynamics in the Antarctic Peninsula Region. *Glob. Planet. Change* **2013**, *100*, 215–223. [CrossRef]
28. Ferreira, A.; Vieira, G.; Ramos, M.; Nieuwendam, A. Ground Temperature and Permafrost Distribution in Hurd Peninsula (Livingston Island, Maritime Antarctic): An Assessment Using Freezing Indexes and TTOP Modelling. *Catena* **2017**, *149*, 560–571. [CrossRef]
29. López-Martínez, J.; Serrano, E.; Schmid, T.; Mink, S.; Linés, C. Periglacial Processes and Landforms in the South Shetland Islands (Northern Antarctic Peninsula Region). *Geomorphology* **2012**, *155–156*, 62–79. [CrossRef]
30. Obu, J.; Westermann, S.; Vieira, G.; Abramov, A.; Balks, M.R.; Bartsch, A.; Hrbáček, F.; Kääb, A.; Ramos, M. Pan-Antarctic Map of near-Surface Permafrost Temperatures at 1 Km^2 Scale. *Cryosph.* **2020**, *14*, 497–519. [CrossRef]
31. Goyanes, G.; Vieira, G.; Caselli, A.; Mora, C.; Ramos, M.; de Pablo, M.A.; Neves, M.; Santos, F.; Bernardo, I.; Gilichinsky, D.; et al. Régimen térmico y variabilidad espacial de la capa active en isla Decepción, Antártida. *Rev. Asoc. Geol. Argent.* **2014**, *71*, 112–124.
32. Ramos, M.; Vieira, G.; de Pablo, M.A.; Molina, A.; Abramov, A.; Goyanes, G. Recent Shallowing of the Thaw Depth at Crater Lake, Deception Island, Antarctica (2006–2014). *Catena* **2017**, *149*, 519–528. [CrossRef]
33. De Pablo, M.A.; Ramos, M.; Molina, A. Snow Cover Evolution, on 2009–2014, at the Limnopolar Lake CALM-S Site on Byers Peninsula, Livingston Island, Antarctica. *Catena* **2017**, *149*, 538–547. [CrossRef]
34. Ramos, M.; de Pablo, M.A.; Molina, A.; Vieira, G.; Trindade, A.; Correia, A. Study of the Active Layer Freezing and Thawing Cycles in the Surroundings of the Spanish Antarctic Station JCI 2000 to 2011. In Proceedings of the 7th Portuguese Spanish Assembly of Geodesy and Geophysics, San Sebastian, Spain, 25–29 June 2012; pp. 723–726.
35. Ramos, M.; Vieira, G.; de Pablo, M.A.; Molina, A.; Jimenez, J.J. Transition from a Subaerial to a Subnival Permafrost Temperature Regime Following Increased Snow Cover (Livingston Island, Maritime Antarctic). *Atmosphere* **2020**, *11*, 1332. [CrossRef]
36. Serrano, E.; Giner, J.; Gumiel, P.; López-Martínez, J. El glaciar rocoso de Hurd: Estructura e inserción en el sistema de transferencia de derrubios Antártico Marítimo (Isla Livington, Islas Shetland de Sur, Antártida). *Rev. Cuat. Geomorfol.* **2004**, *18*, 13–24.
37. Hauck, C.; Vieira, G.; Gruber, S.; Blanco, J.; Ramos, M. Geophysical Identification of Permafrost in Livingston Island, Maritime Antarctica. *J. Geophys. Res.* **2007**, *112*, F02S19. [CrossRef]
38. Recondo, C.; Corbea-Pérez, A.; Peón, J.; Pendás, E.; Ramos, M.; Calleja, J.F.; de Pablo, M.Á.; Fernández, S.; Corrales, J.A. Empirical Models for Estimating Air Temperature Using MODIS Land Surface Temperature (and Spatiotemporal Variables) in the Hurd Peninsula of Livingston Island, Antarctica, between 2000 and 2016. *Remote Sens.* **2022**, *14*, 3206. [CrossRef]

39. Westoby, M.J.; Brasington, J.; Glasser, N.F.; Hambrey, M.J.; Reynolds, J.M. "Structure-from-Motion" Photogrammetry: A Low-Cost, Effective Tool for Geoscience Applications. *Geomorphology* **2012**, *179*, 300–314. [CrossRef]

40. Snavely, N.; Seitz, S.M.; Szeliski, R. Modeling the World from Internet Photo Collections. *Int. J. Comput. Vis.* **2008**, *80*, 189–210. [CrossRef]

41. Javernick, L.; Brasington, J.; Caruso, B. Modeling the Topography of Shallow Braided Rivers Using Structure-from-Motion Photogrammetry. *Geomorphology* **2014**, *213*, 166–182. [CrossRef]

42. Cook, K.L. An Evaluation of the Effectiveness of Low-Cost UAVs and Structure from Motion for Geomorphic Change Detection. *Geomorphology* **2017**, *278*, 195–208. [CrossRef]

43. Furukawa, Y.; Ponce, J. Accurate, Dense, and Robust Multi-View Stereopsis. In Proceedings of the IEEE Computer Society Conference on Computer Vision and Pattern Recognition, Minneapolis, MN, USA, 17–22 June 2007.

44. Lillesand, T.; Kiefer, R.W.; Chipman, J. *Remote Sensing and Image Interpretation*, 7th ed.; Wiley: Hoboken, NJ, USA, 2015; ISBN 9781118919453.

45. Prates, G.; Torrecillas, C.; Berrocoso, M.; Goyanes, G.; Vieira, G. Deception Island 1967–1970 Volcano Eruptions from Historical Aerial Frames and Satellite Imagery (Antarctic Peninsula). *Remote Sens.* **2023**, *15*, 2052. [CrossRef]

46. Tao, C.V.; Hu, Y. A Comprehensive Study of the Rational Function Model for Photogrammetric Processing. *Photogramm. Eng. Remote Sens.* **2001**, *67*, 1347–1358.

47. Marí, R.; de Franchis, C.; Meinhardt-Llopis, E.; Anger, J.; Facciolo, G. A Generic Bundle Adjustment Methodology for Indirect RPC Model Refinement of Satellite Imagery. *Image Process. Line* **2021**, *11*, 344–373. [CrossRef]

48. Howat, I.M.; Porter, C.; Smith, B.E.; Noh, M.J.; Morin, P. The Reference Elevation Model of Antarctica. *Cryosphere* **2019**, *13*, 665–674. [CrossRef]